AIAA AVIATION Forum
12-16 June 2023, San Diego, CA and Online
AIAA AVIATION 2023 Forum

10.2514/6.2023-3567

RBF-FD-based global resolvent analysis: the Blasius boundary layer

Tianyi Chu* and Oliver T. Schmidt†
Department of Mechanical and Aerospace Engineering, Jacobs School of Engineering, UCSD, 9500 Gilman Drive, La Jolla, CA 92093-0411, USA

A high-order mesh-free hydrodynamic stability analysis framework is developed based on radial basis function-based finite differences (RBF-FD). The global linearized Navier-Stokes operator is discretized using polyharmonic spline RBFs with polynomial augmentation (PHS+poly). As a validation test case, the non-parallel flat-plate boundary layer within a computational domain corresponding to a local Reynolds number of $0 \leq \mathrm{Re}_x \leq 6 \times 10^5$ is considered. The computational domain is discretized using scattered nodes created by an unstructured mesh generator. The discrete resolvent operator is constructed, and its singular components are analyzed. The resulting optimal response modes are identified as Tollmien-Schlichting (TS) wavepackets. These responses are optimally forced by the upstream tilted structures that leverage the Orr mechanism. Favorable comparisons to previous literature, both qualitatively and quantitatively, validate the novel framework.

I. Nomenclature

$\mathcal{L}_{\boldsymbol{U}}$, $\boldsymbol{L}_{\boldsymbol{U}}$	=	linearized Navier-Stokes operator around the base-flow and its discretization
$\boldsymbol{A}$	=	RBF-based interpolation matrix
$\mathcal{B}$, C	=	operator for input/output
$\boldsymbol{D}$	=	global RBF-based differentiation matrix
d_f, d_u	=	energy density functions for forcings and responses
Δr	=	local characteristic distance of the grid
$\mathrm{d}V$	=	local control area of the grid
$\boldsymbol{f}$	=	input/forcing vector, local and global
F	=	Normalized frequency
γ	=	RBF interpolation coefficients
$\mathcal{H}$, $\boldsymbol{H}$	=	resolvent operator and its discretization
$\mathcal{L}$	=	linear operator
m	=	exponent of the polyharmonic spline
n	=	local stencil size
N	=	total amount of nodes
∇	=	gradient operator
p	=	pressure
$\mathcal{P}$, $\boldsymbol{P}$	=	prolongation operator and its discretization
$P(\boldsymbol{x})$	=	multivariate polynomial
q	=	degree of the polynomial augmentation
$\phi(r)$	=	radial function
$\boldsymbol{R}$	=	discretized weighted resolvent operator
Re_x, Re_δ	=	Reynolds numbers based on the length of the plate or the displacement thickness
σ	=	resolvent singular value
u, v	=	horizontal and vertical velocity components
$\boldsymbol{u}$	=	velocity vector, local and global
$(\boldsymbol{U}, P)$	=	base flow component
w	=	local RBF weights

*Graduate Student, Department of Mechanical and Aerospace Engineering, Member AIAA.
†Associate Professor, Department of Mechanical and Aerospace Engineering, Senior Member AIAA.

$\boldsymbol{W}_f$, $\boldsymbol{W}_u$ = integration weight matrices
ω = angular frequency
$\boldsymbol{x}$ = node location

II. Introduction

Flow instabilities and large-scale coherent structures are ubiquitous phenomena in fluid mechanics that have been the focus of extensive research. In the past century, local linear stability analysis has been widely used to investigate the growth of small perturbations in laminar flows, e.g., [1–5]. Jackson [6] and Zebib [7] were among the pioneers who performed linear stability analysis in two-dimensional domains to investigate the vortex-shedding characteristics in the wakes of bluff bodies. Readers are referred to Huerre and Monkewitz [8] for a comprehensive review of global stability analysis. Later, linear global analysis has been used to analyze a wide range of flows, including cylinder wakes [9–11], thin aerofoil wakes [12], boundary layers [13], and jets [14], where local analysis is not adequate. It has been shown that an open flow can exhibit global linear stability despite displaying local convective instability. Subsequently, global weakly nonlinear analysis was performed to characterize the dynamics of open flows with strong non-parallelism [15, 16].

More recently, resolvent, or input-output analysis, has revealed its potential to accurately predict large-scale coherent structures in a wide range of flows. The resolvent operator of the forced linearized system constitutes the transfer function between external forcing and the system's response. When applied to laminar flows, resolvent analysis has been used to examine the linear response to external body forces and perturbations for channel flows [17, 18], boundary layers [19–25], and jets [26–28]. Within the turbulent regime, the input-output perspective provides a mathematically consistent framework for analyzing turbulent mean-flows by identifying the forcing with the Reynolds stresses in the perturbation-interaction terms in the Reynolds-decomposed Navier–Stokes equations [29, 30]. Examples include near-wall flows [29–31], boundary layers [32–34], incompressible [26] and compressible jets [27, 35, 36], and the flow over an airfoil [37]. The major challenge for global stability, or resolvent, analysis remains the construction of the underlying large stability matrices in complex domains that have to be decomposed into their eigen- or singular-components.

This work introduced a mesh-free hydrodynamic stability analysis framework tailored for complex geometries, which utilizes radial basis functions (RBFs) to construct large, sparse operators. By generalizing the classical finite-difference (FD) methods to arbitrary node layouts, the RBF-FD methods provide a systematic way to approximate spatial derivatives based on RBFs [38]. This method facilitates maximum flexibility in meshing complex geometries, local grid refinement, and local adjustments of the order of accuracy. Gaussian (GA), multiquadric (MQ), and inverse multiquadric (IMQ) are widely used RBFs for fluid flow problems. These RBFs all involve a shape parameter as a free parameter in the computation, significantly impacting both numerical stability and accuracy. Recently, RBF-FD approximations based on polyharmonic splines (PHS) that are augmented with polynomials (PHS+poly), which were first introduced in Flyer et al. [39], have revealed their potential to achieve high-order accuracy. The accuracy and stability of the PHS+poly RBF-FD method depend on the combination of the stencil size, PHS exponent, and the polynomial degree. Optimal combinations of parameters have been investigated and discussed in Shankar and Fogelson [40], Chu and Schmidt [41], and Le Borne and Leinen [42]. PHS+poly RBF-FDs have succeeded in simulating incompressible flows on scattered nodes [41, 43–46]. In our previous study [47], we employed this discretization method to perform mesh-free global stability and resolvent analyses on the incompressible cylinder wake within the 2-D laminar regime as the first test problem.

Building upon our previous work, we here consider a significantly more challenging case of the non-parallel flat-plate boundary layer. The latter is a classic example of a convectively unstable flow characterized by the amplification of disturbances during downstream advection. The convective instability of boundary-layer flows has been comprehensively studied via local linear stability analysis in the past century, e.g., [48–52]. It has been shown that Tollmien–Schlichting (TS) waves manifest as unstable eigenmodes of the Orr–Sommerfeld equation. While these locally unstable waves are damped within the global framework [13, 53, 54], investigations into the non-normality of the linearized Navier–Stokes equations for open flows have demonstrated an alternative pathway for disturbance amplification [15, 55]. To analyze the non-modal behavior of boundary-layer flows, the global input-output analysis has been conducted to determine the optimal harmonic forcing that results in the largest asymptotic response [19, 20, 56–59]. The response flow field consists of a TS wave packet, and the optimal forcing materializes as an upstream-located tilted wave train that suggests the presence of the Orr mechanism. The TS and Orr mechanisms engage in a competitive interplay while simultaneously contributing to the overall energy gain Sipp and Marquet [20].

As a validation test case, we adopt the configuration proposed by Sipp and Marquet [20], which entails a flat-plate

boundary layer characterized by a Reynolds number of $\mathrm{Re} = 6\times10^5$, or $\mathrm{Re}_\delta = 1332$ based on the displacement thickness, at the end of the optimization domain. The asymptotic Blasius solution is used as the base flow to investigate flow instabilities through the proposed mesh-free resolvent analysis.

III. Radial basis function-based finite differences (RBF-FD)

The goal of the RBF-FD method is to compute the discrete representation of any linear differentiation operator $\mathcal{L}$ at a given location x_0 as a linear combination of the function values, $g(\boldsymbol{x}_j)$, such that

$$\mathcal{L}g(\boldsymbol{x}_0) = \sum_{j=1}^{n} w_j g(\boldsymbol{x}_j). \tag{1}$$

To obtain the unknown differentiation weights w_j, we use the RBF interpolant,

$$s(\boldsymbol{x}) = \sum_{j=1}^{n} \gamma_j \phi(\|\boldsymbol{x} - \boldsymbol{x}_j\|), \tag{2}$$

to approximate the given function $g(\boldsymbol{x})$ by satisfying

$$s(\boldsymbol{x}_j) = g(\boldsymbol{x}_j), \qquad j = 1, 2, \cdots n. \tag{3}$$

Here, $\phi(r)$ is a smooth radial function, $\{\boldsymbol{x}\}_{j=1}^{n}$ is a set of scattered nodes, and $\|\cdot\|$ denotes the standard Euclidean norm. Combining equations (1-3) leads to the linear system

$$\underbrace{\begin{bmatrix} \phi(\|\boldsymbol{x}_1-\boldsymbol{x}_1\|) & \phi(\|\boldsymbol{x}_1-\boldsymbol{x}_2\|) & \cdots & \phi(\|\boldsymbol{x}_1-\boldsymbol{x}_n\|) \\ \phi(\|\boldsymbol{x}_2-\boldsymbol{x}_1\|) & \phi(\|\boldsymbol{x}_2-\boldsymbol{x}_2\|) & \cdots & \phi(\|\boldsymbol{x}_2-\boldsymbol{x}_n\|) \\ \vdots & \vdots & & \vdots \\ \phi(\|\boldsymbol{x}_n-\boldsymbol{x}_1\|) & \phi(\|\boldsymbol{x}_n-\boldsymbol{x}_2\|) & \cdots & \phi(\|\boldsymbol{x}_n-\boldsymbol{x}_n\|) \end{bmatrix}}_{\boldsymbol{A}} \begin{bmatrix} w_1 \\ w_2 \\ \vdots \\ w_n \end{bmatrix} = \begin{bmatrix} \mathcal{L}\phi(\|\boldsymbol{x}-\boldsymbol{x}_1\|)\big|_{\boldsymbol{x}=\boldsymbol{x}_0} \\ \mathcal{L}\phi(\|\boldsymbol{x}-\boldsymbol{x}_2\|)\big|_{\boldsymbol{x}=\boldsymbol{x}_0} \\ \vdots \\ \mathcal{L}\phi(\|\boldsymbol{x}-\boldsymbol{x}_n\|)\big|_{\boldsymbol{x}=\boldsymbol{x}_0} \end{bmatrix}, \tag{4}$$

which can be solved directly to obtain the weight vector $\boldsymbol{w} = [w_1, \cdots, w_n]^T$. An implicit assumption for equation (4) is that the derivative of the basis function, $\mathcal{L}\phi$, is continuous.

A. RBF-FD method with polynomial augmentations

Polynomial augmentation is commonly applied to the RBF-FD method to enforce consistency with Taylor expansion-based FD approximations [39, 60–63]. The two-dimensional augmented RBF-FD method takes the form

$$\mathcal{L}g(\boldsymbol{x}_0) = \sum_{j=1}^{n} w_j g(\boldsymbol{x}_j) + \sum_{i=1}^{(q+1)(q+2)/2} c_i P_i(\boldsymbol{x}_0), \tag{5}$$

where $P_i(\boldsymbol{x})$ are multivariate polynomials up to degree q. To match with the local Taylor series, additional constraints for the differentiation weights,

$$\sum_{j=1}^{n} w_j P_i(\boldsymbol{x}_j) = \mathcal{L}P_i(\boldsymbol{x}_0) \qquad \text{for } 1 \le i \le \frac{(q+1)(q+2)}{2}, \tag{6}$$

are included in the computation.

The use of the above constraints, also known as the vanishing momentum conditions [64], ensures that the RBF approximations locally replicate polynomial behaviour up to degree q [65] and decay in the far-field [66]. A more general and compact representation of equations (5-6) are

$$\begin{bmatrix} \boldsymbol{A} & \boldsymbol{P} \\ \boldsymbol{P}^T & \boldsymbol{0} \end{bmatrix} \begin{bmatrix} \boldsymbol{w} \\ \boldsymbol{c} \end{bmatrix} = \begin{bmatrix} \mathcal{L}\boldsymbol{\phi} \\ \mathcal{L}\boldsymbol{P} \end{bmatrix}, \tag{7}$$

where $\boldsymbol{A}$ is the same interpolation matrix as previously defined in equation (4). Only the weight vector $\boldsymbol{w}$ is used in equation (1) to approximate the differentiation operator $\mathcal{L}$. Motivated by recent studies (see, e.g., [39, 65, 67, 68]), we use polyharmonic splines (PHS),

$$\phi(r) = r^m, \tag{8}$$

as the basis functions, where m is an odd positive integer. The remainder of this paper is dedicated to constructing the discrete linearized Navier-Stokes (LNS) and then resolvent operators using PHS+poly RBF-FDs.

IV. RBF-FD-based global hydrodynamic stability analysis for incompressible flows

A. Governing equations

The motion of a general incompressible Newtonian fluid is governed by the Navier-Stokes equations,

$$\frac{\partial \boldsymbol{u}}{\partial t} + (\boldsymbol{u} \cdot \nabla)\, \boldsymbol{u} = -\nabla p + \mathrm{Re}^{-1} \nabla^2 \boldsymbol{u}, \tag{9a}$$

$$\nabla \cdot \boldsymbol{u} = 0, \tag{9b}$$

All variables are nondimensionalized by the velocity scale $\boldsymbol{U}_\infty$ and the length scale L, and Re denotes the Reynolds number. Within the laminar regime, we decompose the flow quantity into a base flow component $(\boldsymbol{U}, P)$, which is a steady-state solution of equation (9), and a fluctuation component $\boldsymbol{q}' = [\boldsymbol{u}', p']$, such that

$$\boldsymbol{u} = \boldsymbol{U} + \boldsymbol{u}', \quad p = P + p'. \tag{10}$$

The resulting governing equation for the fluctuations can be written compactly as

$$\frac{\partial}{\partial t} \begin{pmatrix} \boldsymbol{u}' \\ 0 \end{pmatrix} = \mathcal{L}_{\boldsymbol{U}} \begin{pmatrix} \boldsymbol{u}' \\ p' \end{pmatrix} + \begin{pmatrix} \boldsymbol{f}' \\ 0 \end{pmatrix}, \tag{11}$$

where

$$\mathcal{L}_{\boldsymbol{U}} \equiv \begin{pmatrix} -(\boldsymbol{U} \cdot \nabla)\,() - [() \cdot \nabla]\, \boldsymbol{U} + \mathrm{Re}^{-1} \nabla^2 & -\nabla \\ \nabla \cdot () & 0 \end{pmatrix} \tag{12}$$

is the linearized Navier-Stokes (LNS) operator around the base flow. The remaining nonlinear interaction

$$\boldsymbol{f}' = -(\boldsymbol{u}' \cdot \nabla)\, \boldsymbol{u}' \tag{13}$$

is generally not negligible of finite amplitude fluctuations and can be interpreted as external forcing to the otherwise linear dynamics. This interpretation was first proposed by McKeon and Sharma [29] for the resolvent framework of turbulent flows.

By assuming a normal mode form for the fluctuating components, $[\boldsymbol{q}',\ \boldsymbol{f}'](\boldsymbol{x}, t) = [\hat{\boldsymbol{q}},\ \hat{\boldsymbol{f}}](\boldsymbol{x}) \mathrm{e}^{\mathrm{i}\omega t} + c.c.$, where ω is the angular frequency, or equivalently by taking the Fourier transform, we obtain the frequency-domain representation of the governing equation (11),

$$\left(\mathrm{i}\omega \mathcal{P}\mathcal{P}^T - \mathcal{L}_{\boldsymbol{U}}\right) \hat{\boldsymbol{q}} = \mathcal{P} \left(\mathcal{B} \hat{\boldsymbol{f}}\right), \tag{14a}$$

$$\hat{\boldsymbol{u}} = \mathcal{P}^T \left(C \hat{\boldsymbol{q}}\right). \tag{14b}$$

Here, $\mathcal{P}$ is the prolongation operator that extends the velocity vector $[u,\ v]^T$ into $[u,\ v,\ 0]^T$, and its transpose is the restriction operator that extracts the velocity vector from the extended state vector. The linear operators $\mathcal{B}$ and C are used to select spatial regions of interest. We write equations (14) in a compact form as

$$\hat{\boldsymbol{u}} = \mathcal{H}(\omega) \hat{\boldsymbol{f}}, \tag{15}$$

where $\mathcal{H}(\omega) = \mathcal{P}^T C \left(\mathrm{i}\omega \mathcal{P}\mathcal{P}^T - \mathcal{L}_{\boldsymbol{U}}\right)^{-1} \mathcal{P}\mathcal{B}$ is known as the resolvent operator. The global operators, such as $\mathcal{L}_{\boldsymbol{U}}$ and $\mathcal{H}$, which arise in both stability and resolvent analyses, can be discretized straightforwardly using differentiation matrices.

B. Global Jacobians and mesh-free hydrodynamic stability analysis

In this work, we leverage the flexibility and accuracy of the PHS+poly RBF-FDs for the construction of differentiation matrices on a set of scattered nodes, $\{\boldsymbol{x}_i\}_{i=1}^N$. For differentiation operators $\mathcal{L} = \frac{\partial^{(\alpha+\beta)}}{\partial x_1^\alpha \partial x_2^\beta}$ in two-dimensional with $\alpha + \beta \leq 2$, we seek differentiation matrices $\boldsymbol{D}_{x_1^\alpha x_2^\beta}$ that satisfy

$$\underbrace{\begin{bmatrix} w_{11} & w_{12} & \cdots & w_{1N} \\ w_{21} & w_{22} & \cdots & w_{2N} \\ \vdots & \vdots & & \vdots \\ w_{N1} & w_{N2} & \cdots & w_{NN} \end{bmatrix}}_{\boldsymbol{D}_{x_1^\alpha x_2^\beta}} \begin{bmatrix} g(\boldsymbol{x}_1) \\ g(\boldsymbol{x}_2) \\ \vdots \\ g(\boldsymbol{x}_N) \end{bmatrix} = \begin{bmatrix} \frac{\partial^{(\alpha+\beta)}}{\partial x_1^\alpha \partial x_2^\beta} g(\boldsymbol{x}_1) \\ \frac{\partial^{(\alpha+\beta)}}{\partial x_1^\alpha \partial x_2^\beta} g(\boldsymbol{x}_2) \\ \vdots \\ \frac{\partial^{(\alpha+\beta)}}{\partial x_1^\alpha \partial x_2^\beta} g(\boldsymbol{x}_N) \end{bmatrix}. \tag{16}$$

Here, (x_1, x_2) are the spatial coordinates. The jth row of the matrix $\boldsymbol{D}$ contains the $n \ll N$ non-zero weights that approximate the derivative at node $\boldsymbol{x}_j$. The resulting matrix is hence sparse $N \times n$ nonzero elements. In a slight change of notation, to enhance readability, we now denote by $\boldsymbol{u} = \boldsymbol{u}(\boldsymbol{x})$ and $\boldsymbol{v} = \boldsymbol{v}(\boldsymbol{x})$ the global velocity fields, and by $\boldsymbol{p} = \boldsymbol{p}(\boldsymbol{x})$ the global pressure field in the computational domain Ω.

Using these differentiation matrices, we assemble the discrete global LNS operator from equation (12) as

$$\boldsymbol{L}_{\boldsymbol{U}} = \begin{pmatrix} \boldsymbol{S} - \mathrm{diag}\left(\boldsymbol{D}_x \boldsymbol{U}\right) + \mathrm{Re}^{-1}\left(\boldsymbol{D}_{xx} + \boldsymbol{D}_{yy}\right) & -\mathrm{diag}\left(\boldsymbol{D}_y \boldsymbol{U}\right) & -\boldsymbol{D}_x \\ -\mathrm{diag}\left(\boldsymbol{D}_x \boldsymbol{V}\right) & \boldsymbol{S} - \mathrm{diag}\left(\boldsymbol{D}_y \boldsymbol{V}\right) + \mathrm{Re}^{-1}\left(\boldsymbol{D}_{xx} + \boldsymbol{D}_{yy}\right) & -\boldsymbol{D}_y \\ \boldsymbol{D}_x & \boldsymbol{D}_y & \boldsymbol{0} \end{pmatrix}, \tag{17}$$

where $\boldsymbol{S} \equiv -\left(\boldsymbol{U} \circ \boldsymbol{D}_x + \boldsymbol{V} \circ \boldsymbol{D}_y\right)$, and $\circ$ denotes the Hadamard product. The discretized form of equation (15) can now be assembled as

$$\hat{\boldsymbol{u}} = \boldsymbol{H}(\omega)\hat{\boldsymbol{f}}, \tag{18}$$

where

$$\boldsymbol{H}(\omega) = \begin{bmatrix} \boldsymbol{1} & \boldsymbol{0} & \boldsymbol{0} \\ \boldsymbol{0} & \boldsymbol{1} & \boldsymbol{0} \end{bmatrix} \boldsymbol{C} \left(\mathrm{i}\omega \begin{bmatrix} \boldsymbol{1} & \boldsymbol{0} & \boldsymbol{0} \\ \boldsymbol{0} & \boldsymbol{1} & \boldsymbol{0} \\ \boldsymbol{0} & \boldsymbol{0} & \boldsymbol{0} \end{bmatrix} - \boldsymbol{L}_{\boldsymbol{U}} \right)^{-1} \begin{bmatrix} \boldsymbol{1} & \boldsymbol{0} \\ \boldsymbol{0} & \boldsymbol{1} \\ \boldsymbol{0} & \boldsymbol{0} \end{bmatrix} \boldsymbol{B} \tag{19}$$

is referred to as the discrete resolvent operator.

Input-output, or resolvent analysis, seeks pairs of optimal forcings and corresponding responses that maximize the gain, σ^2, defined as the ratio of the energy of the response to the energy of the forcing,

$$\sigma^2(\hat{\boldsymbol{f}}; \omega) = \frac{\|\hat{\boldsymbol{u}}\|_u^2}{\|\hat{\boldsymbol{f}}\|_f^2} = \frac{\left\langle \boldsymbol{H}(\omega)\hat{\boldsymbol{f}}, \boldsymbol{H}(\omega)\hat{\boldsymbol{f}} \right\rangle_u}{\left\langle \hat{\boldsymbol{f}}, \hat{\boldsymbol{f}} \right\rangle_f}. \tag{20}$$

The energy of the response and the forcing are measured in the norms $\|\cdot\|_u$ and $\|\cdot\|_f$, induced by the inner products

$$\langle \hat{\boldsymbol{u}}_1, \hat{\boldsymbol{u}}_2 \rangle_u = \hat{\boldsymbol{u}}_2^* \boldsymbol{W}_u \hat{\boldsymbol{u}}_1 \qquad \text{and} \qquad \left\langle \hat{\boldsymbol{f}}_1, \hat{\boldsymbol{f}}_2 \right\rangle_f = \hat{\boldsymbol{f}}_2^* \boldsymbol{W}_f \hat{\boldsymbol{f}}_1 \tag{21}$$

on the output and input spaces, respectively. We further define the modified, or weighted, resolvent operator

$$\boldsymbol{R}(\omega) \equiv \boldsymbol{W}_u^{\frac{1}{2}} \boldsymbol{H}(\omega) \boldsymbol{W}_f^{-\frac{1}{2}} = \tilde{\boldsymbol{U}} \boldsymbol{\Sigma} \tilde{\boldsymbol{F}}^* \tag{22}$$

to account for the kinetic energy on the input and output spaces. The optimal input forcings, $\hat{\boldsymbol{f}}_j$, are determined as the solutions of the eigenvalue problem

$$\boldsymbol{W}_f^{-1} \boldsymbol{H}(\omega)^* \boldsymbol{W}_u \boldsymbol{H}(\omega) = \sigma_j^2 \hat{\boldsymbol{f}}_j. \tag{23}$$

The optimal input and output modes are related through

$$\boldsymbol{R}(\omega)\hat{\boldsymbol{f}}_j = \sigma_j(\omega)\hat{\boldsymbol{u}}_j, \tag{24}$$

which provides a physical interpretation of the singular values and vectors. The response and forcing modes are orthogonal in their respective inner products, that is, $\langle \hat{\boldsymbol{u}}_j, \hat{\boldsymbol{u}}_k \rangle_u = \left\langle \hat{\boldsymbol{f}}_j, \hat{\boldsymbol{f}}_k \right\rangle_f = \delta_{jk}$, and are ordered by their corresponding singular values, σ_j.

V. Application to Blasius boundary-layer flow

We consider a two-dimensional Blasius boundary layer developing over a flat plate with a local Reynolds number of $\mathrm{Re}_x = U_\infty x/\nu \in \left[0, 6\times10^5\right]$ or $\mathrm{Re}_\delta = U_\infty\delta(x)/\nu \in [0, 1332]$ for $x \in [0, 1]$. Here, x is the distance from the leading edge, and $\delta(x) = 1.72\sqrt{\nu x/U_\infty}$ is the displacement thickness of the asymptotic Blasius similarity solution. Above the critical Reynolds number of $\mathrm{Re}_{\delta,c} \approx 520$, this boundary-layer flow exhibits convective instability due to the Orr and Tollmien–Schlichting (TS) mechanisms [48, 50]. Hereafter, we use the notations $\mathrm{Re} = \mathrm{Re}_{x=1}$ and $\delta = \delta(x = 1)$ for simplicity.

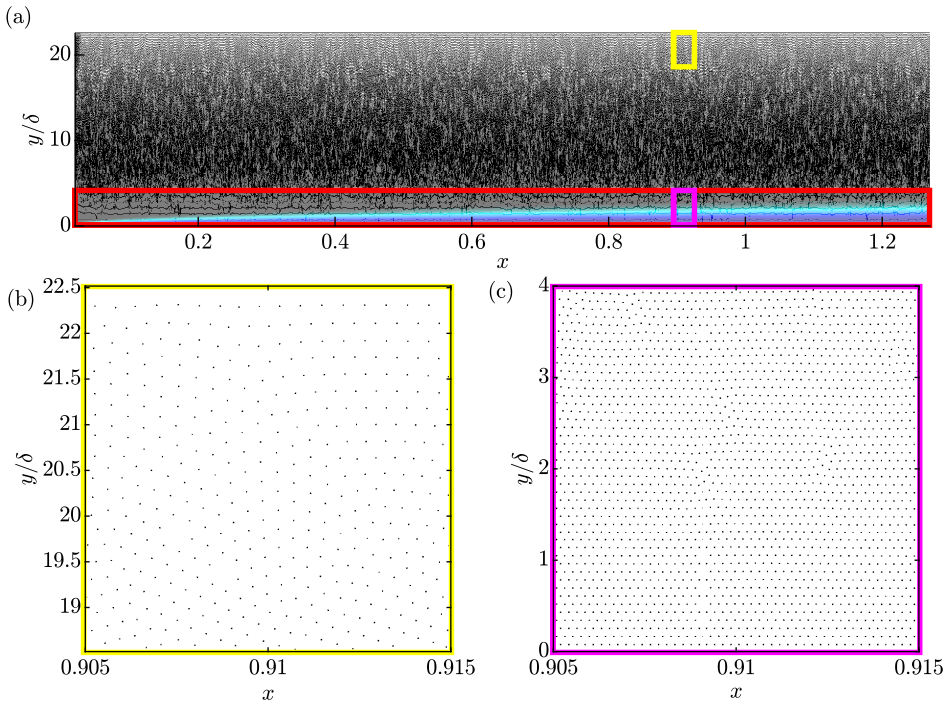

Fig. 1 Global (a) and local (b,c) computational grids. The spatial location of panels (b) and (c) are highlighted as yellow and magenta boxes in panel (a), respectively. For the following figures, we only depict the near-wall region within the red box, see, e.g., figure 4. The flow instability is investigated specifically within the red box (see figure 4 below).

The computational domain, $\Omega \in [0.02, 1.27] \times [0, 0.05]$, is discretized using $N = 726143$ scattered nodes, corresponding to 2.2×10^6 degrees of freedom. In comparison, Sipp and Marquet [20] employs degrees of freedom of 13.7×10^6. The characteristic distances of the grid are $\Delta r = 0.069\delta$ near the flat plate ($y/\delta < 4$), $\Delta r = 0.077\delta$ near the inlet ($x < 0.025$), and average at 0.081δ over the whole domain. The calculation of Δr follows Chu and Schmidt [41]. Local node distributions are shown in figure 1. The leading edge ($x < 0.02$) is removed to avoid the singularity of the Blasius solution. Homogeneous boundary conditions are prescribed on the inlet and the flat plate. Symmetric boundary condition with $v' = \partial u'/\partial y = 0$ is applied at the far-field. A stress-free outflow condition, $-p'\boldsymbol{n} + \mathrm{Re}^{-1}\nabla\boldsymbol{u}'\cdot\boldsymbol{n} = 0$, where $\boldsymbol{n} = [1, 0]^T$ is the outflow direction, is enforced at the outflow.

Following the set up by Sipp and Marquet [20], we also restrict the stability analysis within the interior domain $x \le 1$ such that the forcing optimizes the ratio between the restricted kinetic energy, $\iint_{x\le1}\left(|\hat{u}|^2 + |\hat{v}|^2\right)\mathrm{d}x\mathrm{d}y$, and the

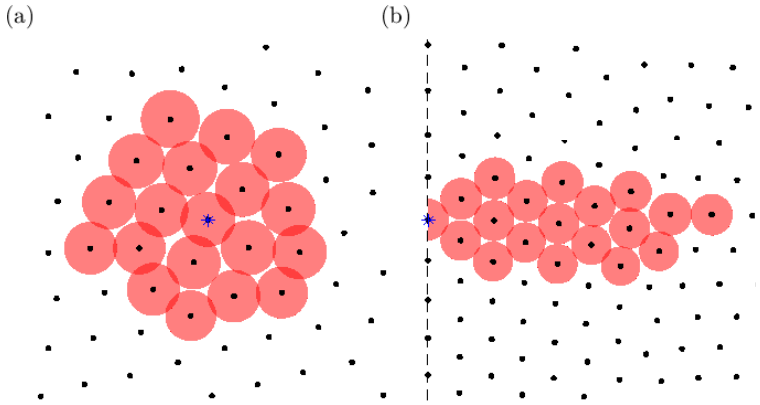

Fig. 2 RBF stencils (red shaded circles) for a given node (blue star): (a) interior nodes; (b) wall-normal derivatives. The stencil size is $n = 19$. The area of each circle represents the corresponding local radial control volume, $\mathrm{d}V_i$.

integral of forcing within the whole computational domain, $\iint_\Omega \left(|\hat{f}_u|^2 + |\hat{f}_v|^2\right) \mathrm{d}x\mathrm{d}y$. In the computation, these two integrals are approximated using the integration matrices

$$\boldsymbol{W}_u = \boldsymbol{W}_f \equiv \begin{bmatrix} 1 & 0 \\ 0 & 1 \end{bmatrix} \otimes \mathrm{diag}(\mathrm{d}V_1, \mathrm{d}V_2, \cdots, \mathrm{d}V_N) \tag{25}$$

in equation (21) to account for the kinetic energy, where $\mathrm{d}V_i \propto \pi(\Delta r_i)^2$ is the local radial control volume for each grid, and $\otimes$ denotes the Kronecker product. In practice, we set $\mathrm{d}V_i$ for $\boldsymbol{W}_u$ to zero if the node $\boldsymbol{x}_i$ lies outside the restricted region. To balance computational efficiency and physical accuracy and ensure stability, the PHS+poly RBF-FDs use a stencil size of $n = 19$, PHS exponent of $m = 3$, and polynomial degree of $q = 2$. Figure 2 shows two examples of RBF stencils used for spatial discretization. For the wall-normal derivatives required for boundary conditions, we employ a specialized stencil that is constructed using a weighted Euclidean distance metric The practical implementation of the PHS+poly RBF-FDs follows Flyer et al. [39].

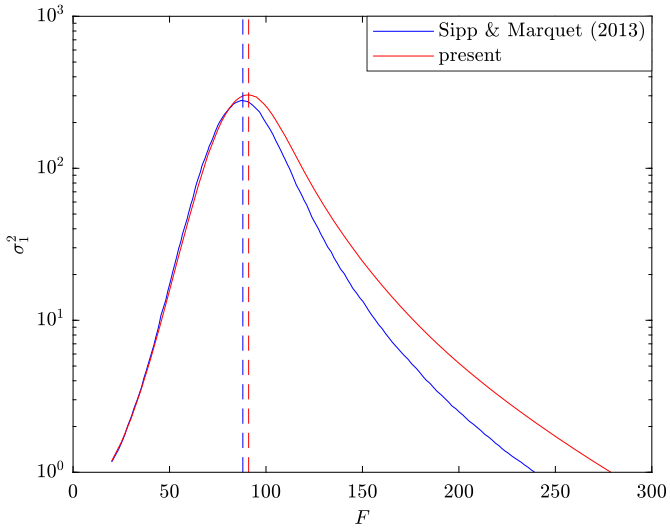

Fig. 3 Resolvent gains (solid lines) and peak frequencies (dashed lines) for the flat-plate boundary layer and $\mathrm{Re} = 6 \cdot 10^5$, compared to previous results by Sipp and Marquet [20] (blue).

We first examine the leading resolvent singular value as a function of the normalized frequency, $F = 10^6 \cdot \omega/\mathrm{Re}$, in figure 3. Favorable agreements are observed between the present results and the one reported by Sipp and Marquet [20] for the overall spectra and their peak values. The slight deviation of the peak and the resolvent gains beyond the peak ($F \gtrsim 88$) are most likely attributed to differences in the base flows, that is, the self-similar Blasius solution in the present study and the fully non-parallel simulation data of Sipp and Marquet [20]. The discrepancy at higher frequencies is potentially also related to the truncation of the leading edge, where the asymptotic Blasius solution becomes singular.

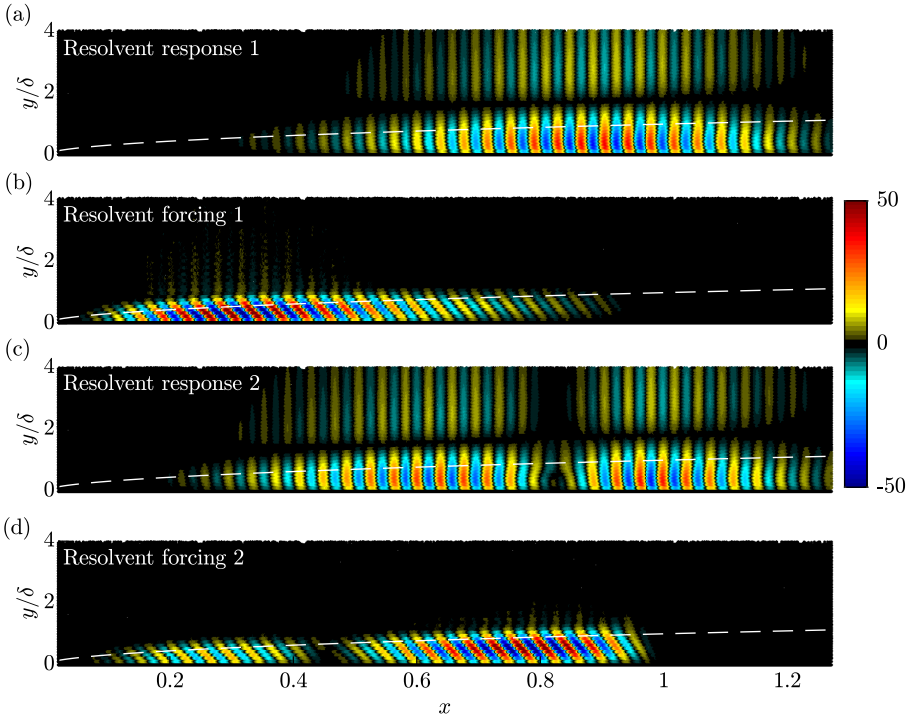

Fig. 4 Optimal and suboptimal resolvent forcings (b,d) and corresponding responses (a,c) at $F = 10^6 \cdot \omega/\mathrm{Re} = 100$. The normalized stream-wise velocity components are shown in $x, y \in [0.02, 1.27] \times [0, 4\delta]$. The Blasius displacement thickness, $\delta(x)$, is highlighted as the white dashed line.

Figure 4 shows the optimal and suboptimal forcings and corresponding responses in terms of the stream-wise velocity at $F = 100$. The optimal response takes the form of Tollmien–Schlichting (TS) wavepackets in the downstream region. The upstream tilted structures in the optimal forcing indicate that the Orr mechanism actively extracts energy from the mean shear via the Reynolds stress [69]. The clear spatial separation between leading resolvent forcing and response modes indicates the streamwise non-normality of the system [15, 70, 71]. The suboptimal forcing and response are similar to the leading modes but exhibit two local maxima. This modulation ensures the orthogonality in their respective inner products. Qualitative comparisons with previous work by Åkervik et al. [13], Monokrousos et al. [19], Brandt et al. [72] and Sipp and Marquet [20] confirm the capability of the present framework for identifying the convective instability of the boundary-layer flow.

As a quantitative assessment of the flow structures, we examine the energy density functions,

$$d_f(x) = \int_0^{y_{\max}} \left(|\hat{f}_u|^2 + |\hat{f}_v|^2 \right) \mathrm{d}y, \qquad \text{and} \qquad d_u(x) = \int_0^{y_{\max}} \left(|\hat{u}|^2 + |\hat{v}|^2 \right) \mathrm{d}y, \tag{26}$$

in figure 5 for the modes shown in figure 4. The present results for both optimal and suboptimal modes are almost identical to those reported by Sipp and Marquet [20], validating the accuracy of the present framework. The spatial distribution of the optimal forcing unambiguously identifies the location of the upstream neutral point (branch I) from a local stability analysis at $x = 0.3$ and the corresponding response is localized at $x = 0.89$, which is in close proximity to the downstream neutral point (branch II).

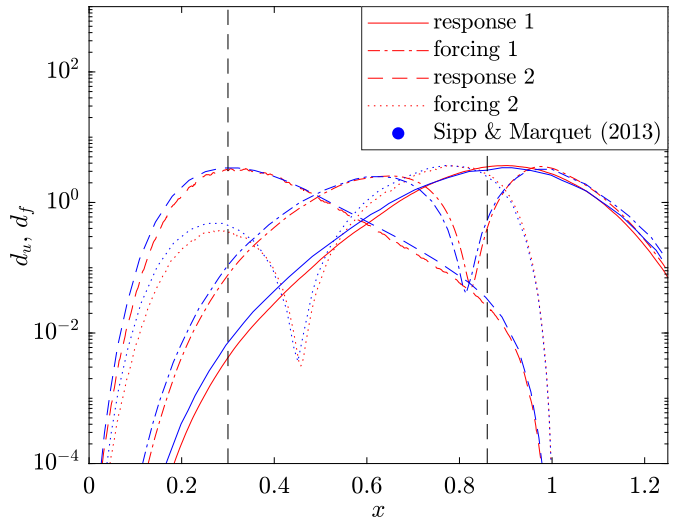

Fig. 5 Spatial distributions of energy density for optimal (dot-dashed) and suboptimal (dotted) forcings and corresponding responses (solid and dashed, respectively) at $F = 100$. The results (red) are compared to those reported by Sipp and Marquet [20] (blue). The two vertical solid lines represent the upstream neutral point (branch I) and the downstream neutral point (branch II) from a local stability analysis.

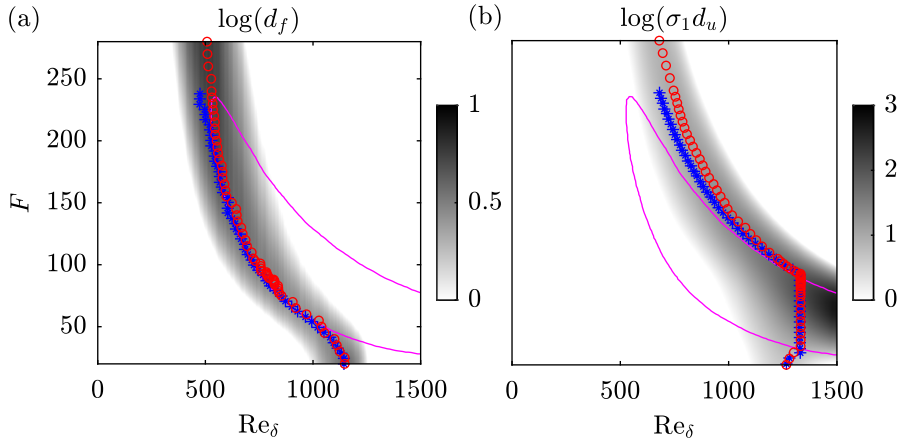

Fig. 6 Energy density distributions for the optimal forcings (a) and responses (b) as a function of frequency. The locations of maximum energy densities are marked as red circles. The results reported by Sipp and Marquet [20] are shown as blue stars for comparison. The neutral curve obtained from a local linear stability analysis is shown as the magenta line.

Figure 6 shows the energy density distributions of the optimal forcing and response as a function of frequency. Here, the stream-wise coordinate is given in terms of the local Reynolds number, $\mathrm{Re}_{\delta(x)}$. The optimal forcings exhibit a high level of agreement with the findings of Sipp and Marquet [20] and their maxima effectively delineate the convectively stable/unstable boundary (branch I) obtained using the local stability theory. The Orr and TS mechanisms coexist and compete while both contributing to the overall energy gain of the global resolvent analysis. The decrease in the spatial support of the Tollmien-Schlichting-like optimal responses with increasing frequencies suggests that only a limited region of the shear layer is capable of supporting the TS mechanism at high frequencies. Similar to the deviation in the resolvent gain spectra shown in figure 3, we observe that the optimal responses peak slightly downstream compared to

the results reported Sipp and Marquet [20] for increasing frequency ($F \gtrsim 130$). However, these discrepancies are minor. Based on the qualitative comparisons presented above, the global mesh-free resolvent analysis is shown to accurately identify the flow instability of the non-parallel flat-plate boundary layer.

VI. Summary

This study validates a novel higher-order mesh-free framework that was specifically developed for hydrodynamic stability analysis. The proposed method employs PHS-type RBFs with polynomial augmentation to discretize large hydrodynamic stability matrix problems on scattered nodes with high accuracy, stability, and computational efficiency. The resulting differentiation matrices are utilized to construct the discrete linearized Navier-Stokes operator for global resolvent analysis. As a validation test case, we considered a non-parallel flat-plate boundary layer in a larger computational domain to fully resolve the Tollmien–Schlichting waves. The leading resolvent modes accurately identify the TS wavepackets that are optimally triggered through the Orr mechanism, as identified by the optimal forcings. The favorable quantitative and qualitative comparisons between the present results and those reported by Sipp and Marquet [20] highlight the feasibility and accuracy of this novel numerical framework.

Acknowledgments

We gratefully acknowledge support by the National Science Foundation under Grant No. CBET-1953999 (PM Ron Joslin).

References

[1] Betchov, R., and Szewczyk, A., "Stability of a shear layer between parallel streams," *Phys. Fluids*, Vol. 6, No. 10, 1963, pp. 1391–1396.

[2] Mattingly, G. E., and Criminale, W. O., "The stability of an incompressible two-dimensional wake," *J. Fluid Mech.*, Vol. 51, No. 2, 1972, pp. 233–272.

[3] Crighton, D. G., and Gaster, M., "Stability of slowly diverging jet flow," *J. Fluid Mech.*, Vol. 77, No. 2, 1976, pp. 397–413.

[4] Ho, C.-M., and Huerre, P., "Perturbed free shear layers," *Annu. Rev. Fluid Mech.*, Vol. 16, No. 1, 1984, pp. 365–422.

[5] Gaster, M., Kit, E., and Wygnanski, I., "Large-scale structures in a forced turbulent mixing layer," *J. Fluid Mech.*, Vol. 150, 1985, pp. 23–39.

[6] Jackson, C. P., "A finite-element study of the onset of vortex shedding in flow past variously shaped bodies," *J. Fluid Mech.*, Vol. 182, 1987, pp. 23–45.

[7] Zebib, A., "Stability of viscous flow past a circular cylinder," *J. Engng Math.*, Vol. 21, No. 2, 1987, pp. 155–165.

[8] Huerre, P., and Monkewitz, P. A., "Local and global instabilities in spatially developing flows," *Annu. Rev. Fluid Mech.*, Vol. 22, No. 1, 1990, pp. 473–537.

[9] Noack, B. R., and Eckelmann, H., "A global stability analysis of the steady and periodic cylinder wake," *J. Fluid Mech.*, Vol. 270, 1994, pp. 297–330.

[10] Pier, B., "On the frequency selection of finite-amplitude vortex shedding in the cylinder wake," *J. Fluid Mech.*, Vol. 458, 2002, pp. 407–417.

[11] Barkley, D., "Linear analysis of the cylinder wake mean flow," *Europhys. Lett.*, Vol. 75, No. 5, 2006, p. 750.

[12] Woodley, B. M., and Peake, N., "Global linear stability analysis of thin aerofoil wakes," *J. Fluid Mech.*, Vol. 339, 1997, pp. 239–260.

[13] Åkervik, E., Ehrenstein, U., Gallaire, F., and Henningson, D. S., "Global two-dimensional stability measures of the flat plate boundary-layer flow," *Eur. J. Mech. B-Fluids*, Vol. 27, No. 5, 2008, pp. 501–513.

[14] Schmidt, O. T., Towne, A., Colonius, T., Cavalieri, A. V., Jordan, P., and Brès, G. A., "Wavepackets and trapped acoustic modes in a turbulent jet: coherent structure eduction and global stability," *J. Fluid Mech.*, Vol. 825, 2017, pp. 1153–1181.

[15] Chomaz, J.-M., "Global instabilities in spatially developing flows: non-normality and nonlinearity," *Annu. Rev. Fluid Mech.*, Vol. 37, 2005, pp. 357–392.

[16] Sipp, D., and Lebedev, A., "Global stability of base and mean flows: a general approach and its applications to cylinder and open cavity flows," *J. Fluid Mech.*, Vol. 593, 2007, pp. 333–358.

[17] Jovanović, M. R., and Bamieh, B., "Componentwise energy amplification in channel flows," *J. Fluid Mech.*, Vol. 534, 2005, pp. 145–183.

[18] Moarref, R., and Jovanović, M. R., "Model-based design of transverse wall oscillations for turbulent drag reduction," *J. Fluid Mech.*, Vol. 707, 2012, pp. 205–240.

[19] Monokrousos, A., Åkervik, E., Brandt, L., and Henningson, D. S., "Global three-dimensional optimal disturbances in the Blasius boundary-layer flow using time-steppers," *J. Fluid Mech.*, Vol. 650, 2010, pp. 181–214.

[20] Sipp, D., and Marquet, O., "Characterization of noise amplifiers with global singular modes: the case of the leading-edge flat-plate boundary layer," *Theor. Comput. Fluid Dyn.*, Vol. 27, No. 5, 2013, pp. 617–635.

[21] Bonne, N., Brion, V., Garnier, E., Bur, R., Molton, P., Sipp, D., and Jacquin, L., "Analysis of the two-dimensional dynamics of a Mach 1.6 shock wave/transitional boundary layer interaction using a RANS based resolvent approach," *J. Fluid Mech.*, Vol. 862, 2019, pp. 1166–1202.

[22] Bugeat, B., Chassaing, J.-C., Robinet, J.-C., and Sagaut, P., "3D global optimal forcing and response of the supersonic boundary layer," *J. Comput. Phys.*, Vol. 398, 2019, p. 108888.

[23] Alizard, F., Gibis, T., Selent, B., Rist, U., and Wenzel, C., "Stochastic receptivity of laminar compressible boundary layers: An input-output analysis," *Phys. Rev. Fluids*, Vol. 7, No. 7, 2022, p. 073902.

[24] Pfister, J.-L., Fabbiane, N., and Marquet, O., "Global stability and resolvent analyses of laminar boundary-layer flow interacting with viscoelastic patches," *J. Fluid Mech.*, Vol. 937, 2022.

[25] Towne, A., Rigas, G., Kamal, O., Pickering, E., and Colonius, T., "Efficient global resolvent analysis via the one-way Navier–Stokes equations," *J. Fluid Mech.*, Vol. 948, 2022, p. A9.

[26] Garnaud, X., Lesshafft, L., Schmid, P. J., and Huerre, P., "The preferred mode of incompressible jets: linear frequency response analysis," *J. Fluid Mech.*, Vol. 716, 2013, pp. 189–202.

[27] Jeun, J., Nichols, J. W., and Jovanović, M. R., "Input-output analysis of high-speed axisymmetric isothermal jet noise," *Phys. Fluids*, Vol. 28, No. 4, 2016, p. 047101.

[28] Semeraro, O., Lesshafft, L., Jaunet, V., and Jordan, P., "Modeling of coherent structures in a turbulent jet as global linear instability wavepackets: theory and experiment," *Int. J. Heat Fluid Flow.*, Vol. 62, 2016, pp. 24–32.

[29] McKeon, B. J., and Sharma, A. S., "A critical-layer framework for turbulent pipe flow," *J. Fluid Mech.*, Vol. 658, 2010, pp. 336–382.

[30] Sharma, A. S., and McKeon, B. J., "On coherent structure in wall turbulence," *J. Fluid Mech.*, Vol. 728, 2013, pp. 196–238.

[31] Hwang, Y., and Cossu, C., "Amplification of coherent streaks in the turbulent Couette flow: an input–output analysis at low Reynolds number," *J. Fluid Mech.*, Vol. 643, 2010, pp. 333–348.

[32] Jacobi, I., and McKeon, B. J., "Dynamic roughness perturbation of a turbulent boundary layer," *J. Fluid Mech.*, Vol. 688, 2011, pp. 258–296.

[33] Bae, H. J., Dawson, S. T. M., and McKeon, B. J., "Resolvent-based study of compressibility effects on supersonic turbulent boundary layers," *J. Fluid Mech.*, Vol. 883, 2020.

[34] Dawson, S. T. M., and McKeon, B. J., "Prediction of resolvent mode shapes in supersonic turbulent boundary layers," *Int. J. Heat Fluid Flow*, Vol. 85, 2020, p. 108677.

[35] Towne, A., Schmidt, O. T., and Colonius, T., "Spectral proper orthogonal decomposition and its relationship to dynamic mode decomposition and resolvent analysis," *J. Fluid Mech.*, Vol. 847, 2018, pp. 821–867.

[36] Schmidt, O. T., Towne, A., Rigas, G., Colonius, T., and Brès, G. A., "Spectral analysis of jet turbulence," *J. Fluid Mech.*, Vol. 855, 2018, pp. 953–982.

[37] Yeh, C.-A., and Taira, K., "Resolvent-analysis-based design of airfoil separation control," *J. Fluid Mech.*, Vol. 867, 2019, pp. 572–610.

[38] Tolstykh, A. I., "On using RBF-based differencing formulas for unstructured and mixed structured-unstructured grid calculations," *Proceedings of the 16th IMACS world congress*, Vol. 228, Lausanne, 2000, pp. 4606–4624.

[39] Flyer, N., Barnett, G. A., and Wicker, L. J., "Enhancing finite differences with radial basis functions: experiments on the Navier–Stokes equations," *J. Comput. Phys.*, Vol. 316, 2016, pp. 39–62.

[40] Shankar, V., and Fogelson, A. L., "Hyperviscosity-based stabilization for radial basis function-finite difference (RBF-FD) discretizations of advection–diffusion equations," *J. Comput. Phys.*, Vol. 372, 2018, pp. 616–639.

[41] Chu, T., and Schmidt, O. T., "RBF-FD discretization of the Navier-Stokes equations on scattered but staggered nodes," *J. Comput. Phys.*, 2022, p. 111756.

[42] Le Borne, S., and Leinen, W., "Guidelines for RBF-FD Discretization: Numerical Experiments on the Interplay of a Multitude of Parameter Choices," *J. Sci. Comput.*, Vol. 95, No. 1, 2023, p. 8.

[43] Shahane, S., Radhakrishnan, A., and Vanka, S. P., "A high-order accurate meshless method for solution of incompressible fluid flow problems," *J. Comput. Phys.*, Vol. 445, 2021, p. 110623.

[44] Shahane, S., and Vanka, S. P., "A semi-implicit meshless method for incompressible flows in complex geometries," *J. Comput. Phys.*, 2022, p. 111715.

[45] Unnikrishnan, A., Shahane, S., Narayanan, V., and Vanka, S. P., "Shear-driven flow in an elliptical enclosure generated by an inner rotating circular cylinder," *Phys. Fluids*, Vol. 34, No. 1, 2022, p. 013607.

[46] Shahane, S., and Vanka, S. P., "Consistency and Convergence of a High Order Accurate Meshless Method for Solution of Incompressible Fluid Flows," *arXiv preprint arXiv:2202.02828*, 2022.

[47] Chu, T., and Schmidt, O. T., "Mesh-free RBF-based discretizations for hydrodynamic stability analysis," *AIAA AVIATION 2022 Forum*, 2022, p. 4098.

[48] Jordinson, R., "The flat plate boundary layer. Part 1. Numerical integration of the Orr—Sommerfeld equation," *J. Fluid Mech.*, Vol. 43, No. 4, 1970, pp. 801–811.

[49] Mack, L. M., "A numerical study of the temporal eigenvalue spectrum of the Blasius boundary layer," *J. Fluid Mech.*, Vol. 73, No. 3, 1976, pp. 497–520.

[50] Smith, F. T., "On the non-parallel flow stability of the Blasius boundary layer," *Proc. R. Soc. London Ser. A*, Vol. 366, No. 1724, 1979, pp. 91–109.

[51] Mack, L. M., "Boundary-layer linear stability theory," Tech. rep., California Inst of Tech Pasadena Jet Propulsion Lab, 1984.

[52] Reed, H. L., Saric, W. S., and Arnal, D., "Linear stability theory applied to boundary layers," *Annu. Rev. Fluid Mech.*, Vol. 28, No. 1, 1996, pp. 389–428.

[53] Ehrenstein, U., and Gallaire, F., "On two-dimensional temporal modes in spatially evolving open flows: the flat-plate boundary layer," *J. Fluid Mech.*, Vol. 536, 2005, pp. 209–218.

[54] Alizard, F., and Robinet, J.-C., "Spatially convective global modes in a boundary layer," *Phys. Fluids*, Vol. 19, No. 11, 2007, p. 114105.

[55] Marquet, O., Lombardi, M., Chomaz, J.-M., Sipp, D., and Jacquin, L., "Direct and adjoint global modes of a recirculation bubble: lift-up and convective non-normalities," *J. Fluid Mech.*, Vol. 622, 2009, pp. 1–21.

[56] Alizard, F., Cherubini, S., and Robinet, J.-C., "Sensitivity and optimal forcing response in separated boundary layer flows," *Phys. Fluids*, Vol. 21, No. 6, 2009, p. 064108.

[57] Bagheri, S., Henningson, D. S., Hoepffner, J., and Schmid, P. J., "Input-output analysis and control design applied to a linear model of spatially developing flows," *Appl. Mech. Rev.*, Vol. 62, No. 2, 2009.

[58] Bagheri, S., Brandt, L., and Henningson, D. S., "Input–output analysis, model reduction and control of the flat-plate boundary layer," *J. Fluid Mech.*, Vol. 620, 2009, pp. 263–298.

[59] Schmid, P. J., Henningson, D. S., and Jankowski, D. F., "Stability and transition in shear flows. applied mathematical sciences, vol. 142," *Appl. Mech. Rev.*, Vol. 55, No. 3, 2002, pp. B57–B59.

[60] Fornberg, B., and Lehto, E., "Stabilization of RBF-generated finite difference methods for convective PDEs," *J. Comput. Phys.*, Vol. 230, No. 6, 2011, pp. 2270–2285.

[61] Fornberg, B., and Flyer, N., "Solving PDEs with radial basis functions," *Acta Numer.*, Vol. 24, 2015, p. 215.

[62] Larsson, E., Lehto, E., Heryudono, A., and Fornberg, B., "Stable computation of differentiation matrices and scattered node stencils based on Gaussian radial basis functions," *SIAM J. Sci. Comput.*, Vol. 35, No. 4, 2013, pp. A2096–A2119.

[63] Wright, G. B., and Fornberg, B., "Scattered node compact finite difference-type formulas generated from radial basis functions," *J. Comput. Phys.*, Vol. 212, No. 1, 2006, pp. 99–123.

[64] Iske, A., "On the approximation order and numerical stability of local Lagrange interpolation by polyharmonic splines," *Modern developments in multivariate approximation*, Springer, 2003, pp. 153–165.

[65] Flyer, N., Fornberg, B., Bayona, V., and Barnett, G. A., "On the role of polynomials in RBF-FD approximations: I. Interpolation and accuracy," *J. Comput. Phys.*, Vol. 321, 2016, pp. 21–38.

[66] Fornberg, B., Driscoll, T. A., Wright, G., and Charles, R., "Observations on the behavior of radial basis function approximations near boundaries," *Comput. Math. with Appl.*, Vol. 43, No. 3-5, 2002, pp. 473–490.

[67] Bayona, V., Flyer, N., Fornberg, B., and Barnett, G. A., "On the role of polynomials in RBF-FD approximations: II. Numerical solution of elliptic PDEs," *J. Comput. Phys.*, Vol. 332, 2017, pp. 257–273.

[68] Bayona, V., Flyer, N., and Fornberg, B., "On the role of polynomials in RBF-FD approximations: III. Behavior near domain boundaries," *J. Comput. Phys.*, Vol. 380, 2019, pp. 378–399.

[69] Butler, K. M., and Farrell, B. F., "Three-dimensional optimal perturbations in viscous shear flow," *Phys. Fluids A*, Vol. 4, No. 8, 1992, pp. 1637–1650.

[70] Marquet, O., Sipp, D., and Jacquin, L., "Sensitivity analysis and passive control of cylinder flow," *J. Fluid Mech.*, Vol. 615, 2008, pp. 221–252.

[71] Sipp, D., Marquet, O., Meliga, P., and Barbagallo, A., "Dynamics and control of global instabilities in open-flows: a linearized approach," *Appl. Mech. Rev.*, Vol. 63, No. 3, 2010.

[72] Brandt, L., Sipp, D., Pralits, J. O., and Marquet, O., "Effect of base-flow variation in noise amplifiers: the flat-plate boundary layer," *J. Fluid Mech.*, Vol. 687, 2011, pp. 503–528.